

# Complete pulse characterization of quantum-dot mode-locked lasers suitable for optical communication up to 160 Gbit/s

H. Schmeckeber, \* G. Fiol, C. Meuer, D. Arsenijević, and D. Bimberg

Institut für Festkörperphysik, Technische Universität Berlin, Hardenbergstrasse 36, 10623 Berlin, Germany

\*schmeckeber@sol.physik.tu-berlin.de

**Abstract:** A complete characterization of pulse shape and phase of a 1.3  $\mu\text{m}$ , monolithic-two-section, quantum-dot mode-locked laser (QD-MLL) at a repetition rate of 40 GHz is presented, based on frequency resolved optical gating. We show that the pulse broadening of the QD-MLL is caused by linear chirp for all values of current and voltage investigated here. The chirp increases with the current at the gain section, whereas larger bias at the absorber section leads to less chirp and therefore to shorter pulses. Pulse broadening is observed at very high bias, likely due to the quantum confined stark effect. Passive- and hybrid-QD-MLL pulses are directly compared. Improved pulse intensity profiles are found for hybrid mode locking. Via linear chirp compensation pulse widths down to 700 fs can be achieved independent of current and bias, resulting in a significantly increased overall mode-locking range of 101 MHz. The suitability of QD-MLL chirp compensated pulse combs for optical communication up to 160 Gbit/s using optical-time-division multiplexing are demonstrated by eye diagrams and autocorrelation measurements.

©2010 Optical Society of America

**OCIS codes:** (140.5960) Semiconductor lasers; (140.4050) Mode-locked lasers; (140.3538) Lasers, pulsed.

---

## References and links

1. P. J. Delfyett, D. H. Hartman, and S. Z. Ahmad, "Optical Clock Distribution Using a Mode-Locked Semiconductor-Laser Diode System," *J. Lightwave Technol.* **9**(12), 1646–1649 (1991).
2. D. Bimberg, M. Grundmann, and N. N. Ledentsov, *Quantum dot heterostructures* (John Wiley, Chichester; New York, 1999), p. 328 p.
3. D. Bimberg, "Quantum dot based nanophotonics and nanoelectronics," *Electron. Lett.* **44**(5), 390 (2008).
4. M. Kuntz, G. Fiol, M. Laemmlin, C. Meuer, and D. Bimberg, "High-speed mode-locked quantum-dot lasers and optical amplifiers," *Proc. IEEE* **95**(9), 1767–1778 (2007).
5. E. U. Rafailov, M. A. Cataluna, and W. Sibbett, "Mode-locked quantum-dot lasers," *Nat. Photonics* **1**(7), 395–401 (2007).
6. M. G. Thompson, A. R. Rae, M. Xia, R. V. Penty, and I. H. White, "InGaAs Quantum-Dot Mode-Locked Laser Diodes," *IEEE J. Sel. Top. Quantum Electron.* **15**, 661–672 (2009).
7. P. Borri, W. Langbein, J. M. Hvam, F. Heinrichsdorff, M. H. Mao, and D. Bimberg, "Spectral hole-burning and carrier-heating dynamics in InGaAs quantum-dot amplifiers," *IEEE J. Sel. Top. Quantum Electron.* **6**(3), 544–551 (2000).
8. S. Schneider, P. Borri, W. Langbein, U. Woggon, R. L. Sellin, D. Ouyang, and D. Bimberg, "Excited-state gain dynamics in InGaAs quantum-dot amplifiers," *IEEE Photon. Technol. Lett.* **17**(10), 2014–2016 (2005).
9. M. Laemmlin, G. Fiol, C. Meuer, M. Kuntz, F. Hopfer, A. R. Kovsh, N. N. Ledentsov, and D. Bimberg, "Distortion-free optical amplification of 20-80 GHz modelocked laser pulses at 1.3  $\mu\text{m}$  using quantum dots," *Electron. Lett.* **42**(12), 697–699 (2006).
10. G. Carpintero, M. G. Thompson, R. V. Penty, and I. H. White, "Low Noise Performance of Passively Mode-Locked 10-GHz Quantum-Dot Laser Diode," *IEEE Photon. Technol. Lett.* **21**(6), 389–391 (2009).
11. D. G. Deppe, H. Huang, and O. B. Shchekin, "Modulation characteristics of quantum-dot lasers: The influence of P-type doping and the electronic density of states on obtaining high speed," *IEEE J. Quantum Electron.* **38**(12), 1587–1593 (2002).

12. G. Fiol, C. Meuer, H. Schmeckebier, D. Arsenijevic, S. Liebich, M. Laemmlin, M. Kuntz, and D. Bimberg, "Quantum-Dot Semiconductor Mode-Locked Lasers and Amplifiers at 40 GHz," *IEEE J. Quantum Electron.* **45**, 1429–1435 (2009).
13. A. R. Kovsh, N. A. Maleev, A. E. Zhukov, S. S. Mikhrin, A. P. Vasil'ev, E. A. Semenova, Y. M. Shernyakov, M. V. Maximov, D. A. Livshits, V. M. Ustinov, N. N. Ledentsov, D. Bimberg, and Z. I. Alferov, "InAs/InGaAs/GaAs quantum dot lasers of 1.3  $\mu\text{m}$  range with enhanced optical gain," *J. Cryst. Growth* **251**(1-4), 729–736 (2003).
14. D. Ouyang, N. N. Ledentsov, D. Bimberg, A. R. Kovsh, A. E. Zhukov, S. S. Mikhrin, and V. M. Ustinov, "High performance narrow stripe quantum-dot lasers with etched waveguide," *Semicond. Sci. Technol.* **18**(12), L53–L54 (2003).
15. R. Trebino, *Frequency Resolved Optical Gating: The Measurement of Ultrashort Laser Pulses* (Kluwer, Boston, 2002).
16. G. P. Agrawal, *Nonlinear fiber optics*, 3 ed. (Academic Press, San Diego, Calif, 2001).
17. L. N. Xu, E. Zeek, and R. Trebino, "Measuring very complex ultrashort pulses using Frequency-Resolved Optical Gating (FROG)," 2008 Conference on Lasers and Electro-Optics & Quantum Electronics and Laser Science Conference, Vols 1–9, 1043–1044 (2008).
18. N. G. Usechak, Y. C. Xin, C. Y. Lin, L. F. Lester, D. J. Kane, and V. Kovanis, "Modeling and Direct Electric-Field Measurements of Passively Mode-Locked Quantum-Dot Lasers," *IEEE J. Sel. Top. Quantum Electron.* **15**, 653–660 (2009).
19. Y. C. Xin, D. J. Kane, and L. F. Lester, "Frequency-resolved optical gating characterisation of passively modelocked quantum-dot laser," *Electron. Lett.* **44**(21), 1255–1256 (2008).
20. T. Piwonski, J. Pulka, G. Madden, G. Huyet, J. Houlihan, E. A. Viktorov, T. Erneux, and P. Mandel, "Intradot dynamics of InAs quantum dot based electroabsorbers," *Appl. Phys. Lett.* **94**(12), 123504 (2009).
21. E. A. Viktorov, P. Mandel, A. G. Vladimirov, and U. Bandelow, "Model for mode locking in quantum dot lasers," *Appl. Phys. Lett.* **88**(20), 201102 (2006).
22. X. D. Huang, A. Stintz, H. Li, A. Rice, G. T. Liu, L. F. Lester, J. Cheng, and K. J. Malloy, "Bistable operation of a two-section 1.3- $\mu\text{m}$  InAs quantum dot laser - Absorption saturation and the quantum confined Stark effect," *IEEE J. Quantum Electron.* **37**(3), 414–417 (2001).
23. O. E. Martinez, J. P. Gordon, and R. L. Fork, "Negative Group-Velocity Dispersion Using Refraction," *J. Opt. Soc. Am. A* **1**(10), 1003–1006 (1984).

## 1. Introduction

The demand for high-speed, short-pulse, optical sources drives the research on GaAs quantum-dot (QD)-based monolithic mode-locked lasers (MLL) as sources for applications such as optical clocking [1] and future all-optical networks like the 100 Gbit/s Ethernet. Due to the QDs size distribution, QD-MLLs exhibit an inhomogeneously broadened gain spectrum [2,3]. As a consequence, theoretically ultrashort pulse widths on the order of a few hundred femtoseconds are achievable [4–6] superior to conventional gain media like bulk or quantum well materials. Additionally, QD-MLLs demonstrated low threshold currents, high  $T_0$  and ultrafast dynamics exhibiting ground state gain recovery of down to 130 fs [7,8]. QD-based fundamental MLLs were realized at low repetition rates of a few GHz up to ultrahigh repetition rates of around 80 GHz [9]. The stability of mode-locking in QD-based devices results in pulse timing jitter down to 190 fs [4,10]. Here we investigate the chirp of QD-MLL, compensate it and demonstrate fs-pulses up to 160 GHz repetition rate.

This paper is organized as follows: In Section II, we describe the epitaxial structure, the device design and modes of operation of the QD-MLL. This is followed by the pulse characterization for different values of current and voltage as well as a comparison of passive and hybrid operation in Section III. Subsequently, in Section IV, the results of pulse compression are presented, followed by the demonstration of the suitability for data transmission up to 160 Gbit/s in Section V. A conclusion is given in Section VI.

## 2. Quantum-dot mode-locked laser

The AlGaAs/GaAs laser structure was grown by molecular beam epitaxy. It imbeds 15 stacks of InGaAs/GaAs QDs. Each QD layer is overgrown with an InGaAs quantum well (dot in a well structure), in order to shift the emission wavelength to 1.31  $\mu\text{m}$ , which represents the center of the O-band in optical communication (ITU-T, G.694). Suitable barrier layers between the QD layers provide strain relaxation and are p-doped to increase the temperature stability [11,12]. More detailed information on the growth can be found in [13].

The mesa consists of a 4- $\mu\text{m}$ -wide ridge waveguide which was processed by dry etching through the active region. Deep etching provides index guiding of the optical mode and a suppression of current spreading [14]. The 1-mm-long cavity of the QD-MLL is composed by two monolithically integrated sections, a 900- $\mu\text{m}$ -long standard biased gain section (SGS) and a 100- $\mu\text{m}$ -long saturable absorber section (SAS). The main advantages of monolithically integrated sections are small footprint, mechanical stability and integrability with other components. The two sections were separated by etching a 20  $\mu\text{m}$  gap into the top metallization and the upper layers without impacting the waveguide. Thus, an electrical resistance of around 10 k $\Omega$  between the p-contacts of the two sections is realized.

The front facet of the SGS is as cleaved and the rear facet (at the SAS side) is high reflection coated. In the absence of bias on the SAS the threshold current density in the SGS is about 360 A/cm<sup>2</sup> at room temperature. Depending on the values of current and reverse bias an average optical power up to 12 mW from the cleaved facet can be achieved during mode locking.

If the SGS and the SAS are dc biased, the mode of operation is called passive mode locking (PML), whereas for hybrid mode locking (HML) an additional radio-frequency signal is provided to the SAS. HML leads to more stable mode locking, as a consequence of a stronger coupling of the longitudinal cavity modes caused by side-band production between the cavity modes and the external signal. The external frequency matches the cavity round-trip time which is near to 40 GHz. Due to the low-jitter external RF signal, we obtain a dramatic decrease of the pulse timing jitter down to around 190 fs [4]. Depending on the values of current, reverse bias and the RF source power, which is limited to + 14 dBm at 40 GHz, we achieved a locking range up to 30 MHz [4].

The QD-MLL chip is packaged into a butterfly module containing a bias tee, an electrical microwave port, a RF impedance matching network for the SAS and a dc contact for the SGS. Furthermore it includes a thermoelectric cooler and thermistor for temperature stability as well as a long-term stable standard-single-mode-fiber (SMF-28) pigtail.

In order to improve the characteristics of the QD-MLL pulses it is mandatory to have access to both, the pulse shape and phase.

### 3. Pulse characterization using frequency resolved optical gating

Characterization of picosecond and sub-picosecond pulses is commonly conducted by second harmonic generation (SHG) autocorrelation (AC) measurements. Since the integrated intensity is detected, any phase information is lost. Retrieving the pulse intensity profile from the convoluted pulse is known as one-dimensional phase-retrieval problem [15], which can only be solved assuming a particular pulse shape (e.g. Gaussian,  $\text{sech}^2$ ). Therefore, SHG-AC measurements only allow an estimate of the pulse width and cannot yield an exact characterization. Using frequency resolved SHG-AC, called SHG frequency resolved optical gating (FROG), a spectrally resolved convoluted intensity versus the time delay can be recorded. Retrieving the pulse shape and phase from this experiment represents a two-dimensional phase-retrieval problem, which can be solved by a numerical algorithm [15]. The result has only a time direction ambiguity which can be unambiguously resolved by simulations of pulse propagation via the split-step algorithm specified in [16] and comparison to additional measurements after introduction of a known amount of dispersion [15]. A highly sensitive SHG-FROG setup consisting of a monochromator (focal length 50 cm, 1600 lines/mm) and an extremely sensitive charge-coupled device (CCD) behind the SHG-AC setup was built, shown in Fig. 1.

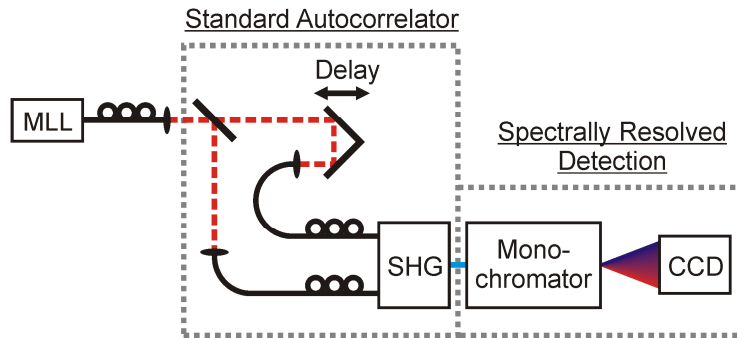


Fig. 1. Sketch of the SHG-FROG setup.

Coincidental to highly resolved SHG-FROG spectrograms (256 x 256 measurement points), our setup shows more than one and a half orders of magnitude dynamic range and low noise for pulses with an energy down to 9 fJ and a peak power of 3.5 mW.

### 3.1 Passive mode locking

A map of proper mode locking as a function of the values of the SGS current and the SAS reverse bias was generated by AC measurements and shows the deconvoluted pulse FWHM in Fig. 2 (Gauss-fit). The color coded area represents stable mode locking, whereas white areas correspond to cw lasing or incomplete mode locking. The corresponding spectral FWHM indicates that the pulses are not Fourier-limited. In principle this could be caused by incomplete locking of the spectral components or by chirp. In the latter case the chirp gradient is decisive, because linear chirp can be compensated easily.

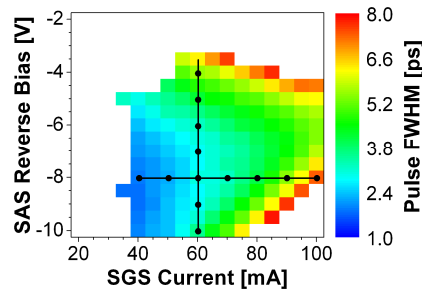


Fig. 2. SGS current and SAS reverse bias dependent pulse FWHM, derived from autocorrelation measurements, assuming a Gaussian pulse shape. Black circles mark the values of the SGS current and the SAS reverse bias investigated by FROG.

FROG measurements for the values of current and reverse bias marked by black circles in the mode-locking map were conducted. The influence of the operating parameters on device dynamics and pulse characteristics is investigated for constant SGS current and increasing SAS reverse bias and vice versa. A FROG spectrogram with color-coded intensity in a logarithmic scale is shown in Fig. 3 for the crossing point of the two lines.

With regards to time delay the spectrogram is symmetric by definition of SHG-autocorrelation. Depending on the operating parameters, the spectrogram becomes smaller, respectively broader, but the general shape stays roughly the same. From this spectrogram, using the algorithm explained above, the pulse intensity profile and the spectrum of the measured comb can be retrieved numerically. As a measure of the validity of the retrieved pulse a root mean square (RMS) FROG retrieval error  $\epsilon$  is given. For all measurements, except at highest SGS currents, this error is less than or equal to 0.007, proving that the results are very reliable [17]. Because the FROG algorithm is based on Fourier-transformations, the SHG intensity has to be zero at the edges of the FROG spectrogram (boundary condition).

Due to the high repetition rate, which gives a maximum time delay of 12.5 ps between consecutive pulses, and the sampling technique of FROG, this cannot be assured for broader pulses, leading to larger retrieval errors at higher SGS currents.

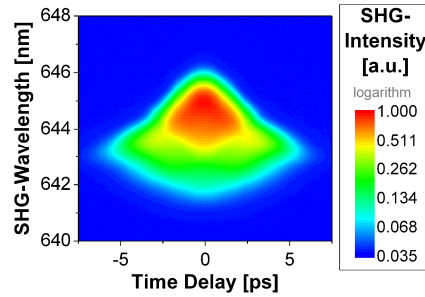


Fig. 3. Measured FROG spectrogram of the passive-mode-locked laser at 60 mA gain section current and  $-8$  V absorber section reverse bias.

The retrieved optical spectra agree well to the spectra measured using an optical spectrum analyzer. This proves that the spectrum is completely locked and the pulse broadening stems from chirp generated within the laser itself. Additionally, the nonlinear behavior of the SHG crystal limits the sensitivity of SHG-FROG to cw fractions of the signal and thus the comparison of the spectra reveals that the cw background is highly suppressed.

Asymmetric as well as nearly symmetric pulse intensity profiles are retrieved depending on the values of current and reverse bias. In all measurements a dominant quadratic temporal phase is observed. Thus the temporal chirp is basically linear. The pulse intensity profile and temporal chirp are shown in Fig. 4 (left) for different SGS currents and in Fig. 4 (right) for different SAS reverse biases. All pulses show nearly the same steeply rising edge (at negative times) formed by the absorption of the SAS, but different trailing edges depending on the values of current and reverse bias. The secondary peak in the asymmetric trailing edges could be caused by saturation effects within the SGS leading to pulse distortion. These saturation effects occur in particular for modes near the gain peak. A reflection as the origin of this peak can be excluded, because the relative temporal position varies for different currents and reverse bias.

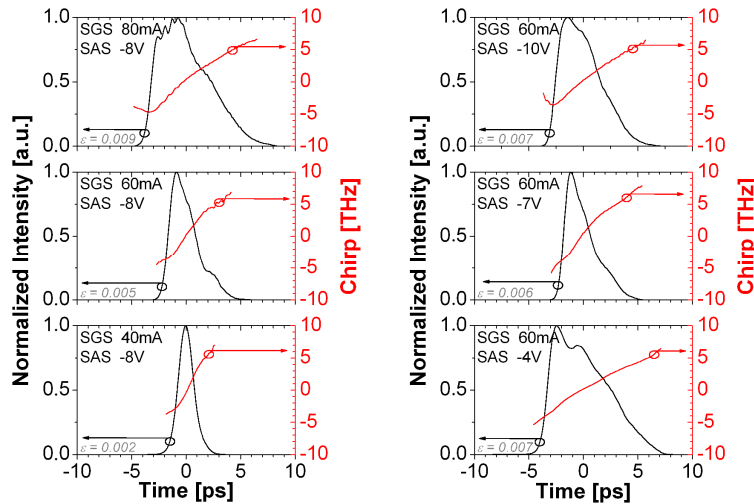


Fig. 4. Retrieved pulse intensity profile and temporal chirp for different SGS currents (left column) and SAS reverse biases (right column) of the passive-mode-locked device including the respective retrieval error  $\epsilon$ .

Due to the small gain at low SGS current, most of the carriers in the QDs are consumed by the leading parts of the pulse. Increasing the SGS current for constant SAS reverse bias leads to larger gain in the cavity and the gain dynamics becomes more pronounced for the pulse shaping. As a consequence a flattening of the trailing edge occurs and the pulse shape becomes asymmetric, consistent with previous measurements in [18,19]. The weak oscillations of the pulse shape for a SGS current of 80 mA are probably caused by the problem of boundary conditions mentioned above or saturation effects induced by the most intense modes.

At low SAS reverse bias, the SAS dynamics is defined by a low saturation power and slow recovery times [20,21]. With increasing SAS reverse bias and constant SGS current the SAS efficiency and as a consequence the absorption rise, resulting in shorter pulses. However, at the largest SAS reverse bias values the pulses become broader again, probably due to the quantum confined stark effect (QCSE) [22]. The QCSE causes a red shift of the SAS absorption spectra compared to the SGS gain spectra leading to a reduced efficiency and pulse shaping effectivity.

In addition to the pulse intensity profile the chirp gives further information about the dynamics. The chirp is determined here for all retrieved pulse intensity profiles from the temporal phase. Calculations have already shown [21], that the change of the carrier density in the wetting layer of a DWELL structure during the pulse amplification in the SGS is linear. Associated with the carrier-density change is a linear change of the refractive index during the pulse, inducing a linear temporal chirp of the pulse. The temporal chirp can be converted to the commonly used spectral chirp. The slope of the linear spectral chirp is plotted together with the pulse FWHM in Fig. 5 (left) for different SGS currents and in Fig. 5 (right) for different SAS reverse biases. We observe pulse FWHM ranging from 1.6 ps to 7.5 ps and a linear spectral chirp from  $-0.37$  ps/nm to  $-1.2$  ps/nm. The FWHM-time-bandwidth product (TBP), which is not displayed here, shows the same trend as the pulse FWHM and ranges from 1.4 to 11.2.

Increasing the SGS current leads to larger spectral chirp which manifests itself in pulse broadening. This is caused by the stronger depletion of the wetting layer due to increasing current and photon density at higher SGS currents.

In contrast, increasing the SAS reverse bias results at first in less spectral chirp and hence narrower pulses. This broadening can be explained by decreasing depletion of the wetting layer with increasing bias due to the higher absorption and therefore a lower photon density in the cavity, which is proven by lower optical output power. This process is stopped and inverted at still higher biases owing to the QCSE inducing lower absorption and therefore again a higher photon density in the cavity [4].

The linear spectral chirp and the pulse FWHM dependence on the values of current and reverse bias exhibit a similar trend showing that they are connected to each other (Fig. 5).

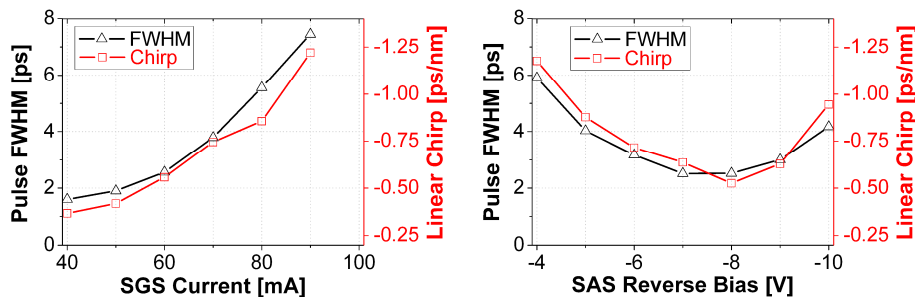


Fig. 5. Retrieved pulse FWHM and linear spectral chirp for varying SGS current at constant SAS reverse bias of  $-8$  V (left) and for varying SAS reverse bias at constant SGS current of 60 mA (right) for passive mode-locking.

It should be mentioned that the dynamics of the carrier density in the SAS and the SGS result in chirp of opposite sign. The SAS induces a positive spectral chirp to the leading part of the pulse, which is normally strongly suppressed due to very effective photon absorption before saturation. The SGS, however, produces negative spectral chirp as stated above.

These results will enable improvements of the mode-locking performance in future device generations. In particular, the SAS can be optimized by enhancing the absorption efficiency via increasing the length or ion implantation of the SAS. Ion implantation also offers a way to reduce the influence of the QCSE.

### 3.2 Hybrid mode locking

In the following measurements of hybrid mode locking are presented for the values of the SGS current and the SAS reverse bias at the cross point of the two lines in Fig. 2. Similar results are obtained at the other operating points we have investigated.

The RF spectra of the PMLL, measured by a photo diode combined with an electrical spectrum analyzer (ESA), show a broad signal peak at the native pulse repetition frequency due to pulse timing jitter as shown in Fig. 6 (left). Switching to hybrid mode locking decreases the jitter dramatically. The HMLL peak becomes almost delta-function like, if the external frequency is within the mode-locking range and the side-band-suppression ratio (SBSR) is larger than 30 dB. If the external frequency is outside of the locking range, other peaks can be observed in the RF spectrum, most probably as a result of four-wave-mixed frequency components of the native pulse repetition rate and the external signal. The external signal remains in all cases a nearly delta-function like peak.

An additional RF signal with a peak-to-peak amplitude of 3.2 V leads to a modulation of the SAS reverse bias around the PMLL SAS reverse bias. Therefore, the voltage in the net-gain window of the SAS is decreasing and due to this the QCSE becomes lower. As a result a blue shift of the HMLL spectra is observed in comparison to the PMLL spectra.

The retrieved pulses of the HMLL are shown in comparison to the PMLL in Fig. 6 (right). It should be noted that the hybrid operating mode shortens the pulse slightly as well as suppresses the shoulder on the trailing edge. This suppression may originate from the fact that for hybrid mode locking the absorption for the trailing part is higher than for the main peak due to the time-dependent RF sine voltage on the SAS.

No differences between the different external frequencies can be observed. But it should be mentioned that it would need a single shot FROG to check, if there are unstable pulses at the edge frequencies. The linear spectral chirp of the HMLL is equal to the PMLL. The FWHM-TBP decreases marginally when switching from PMLL to HMLL. In conclusion, hybrid mode locking has a small influence on the pulse shape and chirp as well as the FWHM-TBP, but a decisive influence on the pulse timing jitter due to temporal stabilization and the faster closing of the net-gain window.

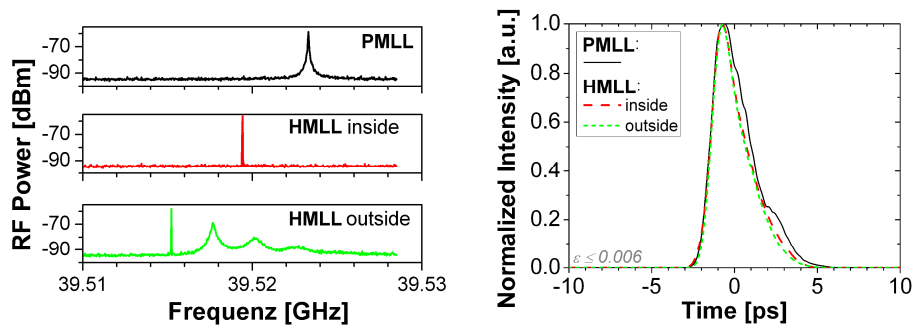


Fig. 6. RF spectra (left) and retrieved pulse intensities with the respective retrieval error  $\epsilon$  (right) of passive-(PMLL) and hybrid-(HMLL) mode-locked device with 60 mA SGS current

and  $-8$  V SAS reverse bias and an external frequency inside and outside of the mode-locking range.

#### 4. Pulse compression

Compensation of the linear chirp using the split-step algorithm [16] for pulse propagation including second-order dispersion effects was calculated. The compensation results in a very flat temporal phase trend across the pulse and an almost vanishing chirp. Theoretically pulse FWHMs in the sub-picosecond range of 530 fs to 620 fs are predicted implying a compression factor of 3 to 14, depending on the values of current and reverse bias.

For an experimental implementation of the chirp compensation, neither SMF-28 nor dispersion-shifted fiber (DSF) can be used, because these fibers have a normal dispersion at the emission wavelength of 1290 nm and hence induce a negative linear spectral chirp to the pulses. In order to generate positive dispersion a tunable free-space-dispersion compensator (FSDC) was set up based on grating and telescope optics [23]. By means of the FSDC the pulses were compensated and again characterized using our SHG-FROG setup. A FROG spectrogram for chirp-compensated PMLL and HMLL at the crossing point of the two lines in Fig. 2 is shown in Fig. 7 (left). The corresponding retrieved pulse intensity profiles and chirps together with the non compensated data are shown in Fig. 7 (right).

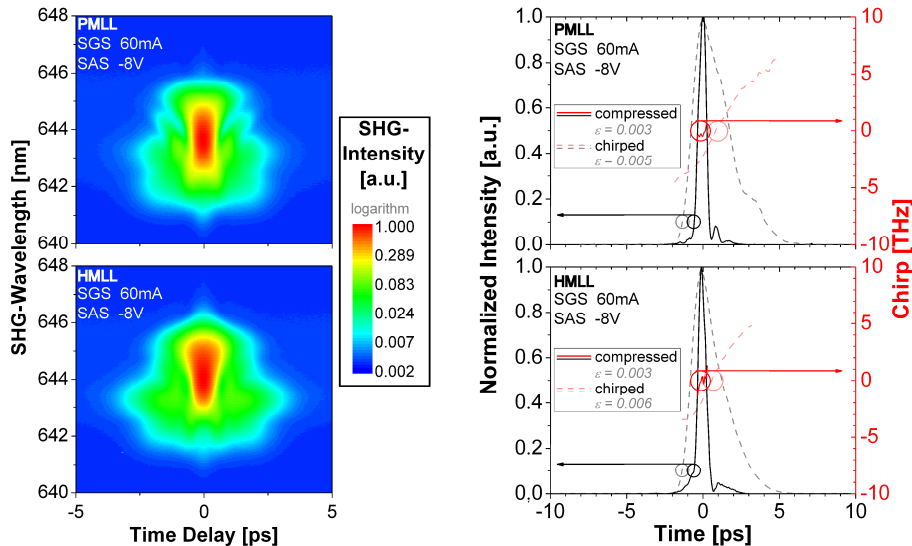


Fig. 7. Experimental measured FROG spectrogram of the chirp-compensated PMLL (left top) and HMLL (left bottom) with 60 mA SGS current and  $-8$  V SAS reverse bias. Corresponding retrieved pulse intensity profiles and chirps with the respective retrieval error  $\epsilon$  together with the chirped pulse intensities and chirps (right).

Both pulses have one trailing pulse which is suppressed by a factor of more than 10 for the PMLL and 20 for the HMLL. The same trailing pulse is also observed in the numerical simulations. The temporal phase is almost flat across the main peak pulse. For the other values of current and reverse bias similar compressed pulses are found. A probable reason for the trailing pulse could be higher order chirp which cannot be compensated by our setup.

The pulse FWHM and the linear spectral chirp for the PMLL are presented in Fig. 8 (left) and in Fig. 8 (right) dependent on the SGS current and on the SAS reverse bias, respectively. The linear spectral chirp varies around zero and is below  $\pm 0.4$  ps/nm, varying within a small adjustment margin.

The most important result is that after pulse compression the pulse FWHM is almost independent of the values of current and reverse bias. The lowest pulse FWHM we observed is 700 fs close to prediction. The experimentally achieved compression factors are slightly

smaller than the simulated ones since the FSDC clips the optical spectrum slightly. The FWHM-TBP is between 0.5 and 0.8.

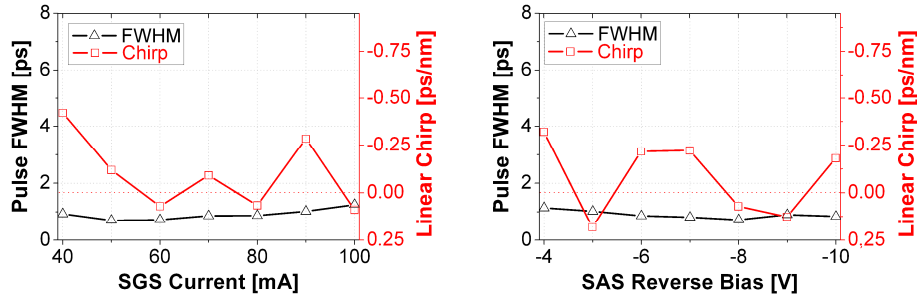


Fig. 8. PMLL retrieved pulse FWHM and linear spectral chirp for varying SGS current at constant SAS reverse bias of  $-8$  V (left) and for varying SAS reverse bias at constant SGS current of  $60$  mA (right) of the pulse compressed passive mode-locked device.

This independence enables us to tune the repetition rate by varying the SGS current and the SAS reverse bias with a negligible change of the pulse FWHM. Consequently, we achieve a significantly larger hybrid mode locking range because the native repetition frequency can be shifted by varying the values of the SGS current and the SAS reverse bias. An overall locking range of  $101$  MHz can be achieved here as shown in Fig. 9.

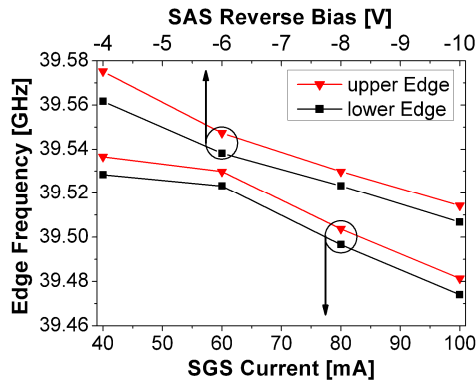


Fig. 9. Edges of the mode-locking range for varying SGS currents at constant SAS reverse bias of  $-8$  V and for varying SAS reverse bias at constant SGS currents of  $60$  mA.

Depending on the values of current and reverse bias the optical average output power in the fiber after the FSDC varies slightly between  $-10.3$  dBm and  $-6.3$  dBm and the pulse peak power between  $2$  mW and  $6$  mW. This variation can be eliminated by a variable attenuator like an electro-absorption attenuator which follows the QD-MLL.

## 5. Optical communication

In order to judge the suitability of our device for high-speed optical communication we set up a transmitter consisting of the QD-MLL and the FSDC followed by an electro-optical modulator which is driven by a bit pattern generator (BPG). The QD-MLL was operated in the hybrid-mode-locking regime to ensure synchronization between the BPG and the pulse comb. The transmitter emits a pseudo-random binary sequence  $2^{31}-1$  (PRBS-31) data stream in a return-to-zero (RZ) format with a data transmission rate of close to  $40$  Gbit/s. The corresponding eye diagram is shown in Fig. 10 (left). A clear open eye can be observed with a signal-to-noise ratio (SNR) of  $19.8$  and a RMS timing jitter of  $342$  fs. In bit error rate (BER) measurements we observe no error floor for BERs of  $10^{-12}$  at receiver powers as low as  $-27$  dBm [12].

To increase the data transmission rate we have built an optical-time-division multiplexer (OTDM). It splits up the data stream, delays one part by the half length of the PRBS and recombines both parts. Therefore, our OTDM converts a PRBS-7 with a data transmission rate of 40 Gbit/s to a true PRBS-7 with a selectable data transmission rate of either 80 Gbit/s or 160 Gbit/s in a second stage. Figure 10 (right) shows the 80 Gbit/s eye diagram. Again a clear open eye can be observed despite the fact that the measurement is limited by the photodiode and the 70-GHz oscilloscope. It shows a SNR of 13.5.

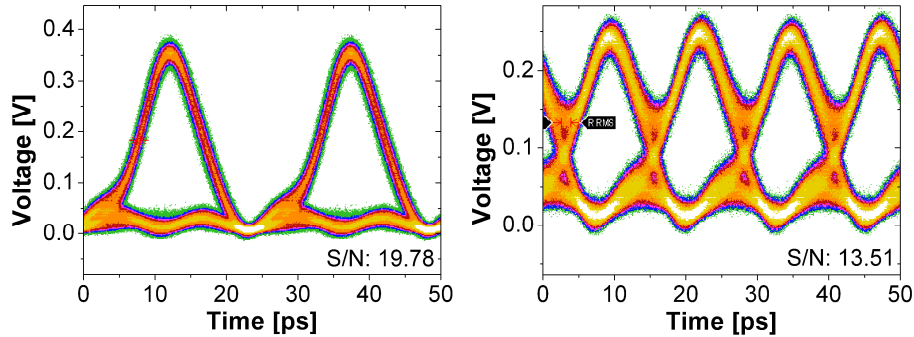


Fig. 10. RZ eye diagram for 40 Gbit/s with PRBS-31 (left) and multiplexed 80 Gbit/s with PRBS-7 (right) of the hybrid-mode-locked device with 80 mA SGS current and  $-8$  V SAS reverse bias.

Figure 11 (left) shows a SHG measurement of an 160-GHz signal and Fig. 11 (right) shows the corresponding retrieved pulse comb from Fig. 7 (right bottom), which is artificially assembled to an 160-GHz-sampling pulse comb. The pulse comb shows distinct pulses. Due to the sampling technique of the SHG measurement already explained above, the SHG measurement shows only nearly distinct peaks with a delay of 6.3 ps according to the basic pulse-repetition frequency of 39.52 GHz. Thus we demonstrate here for the first time that a two section 40 GHz QD-MLL at  $1.3 \mu\text{m}$  is suitable for generating optical data streams by time-division multiplexing up to 160 Gbit/s.

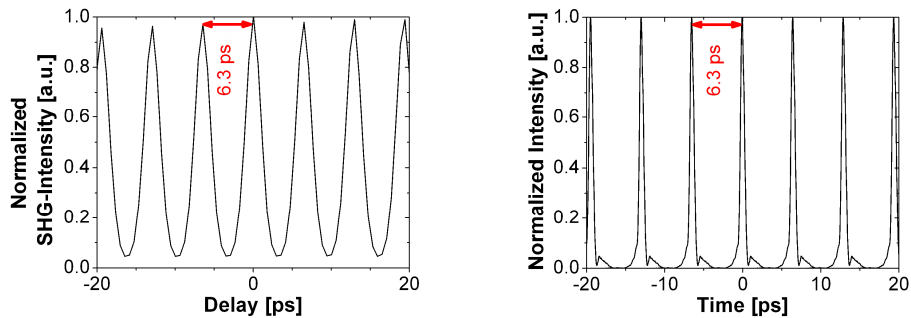


Fig. 11. Autocorrelation measurement (left) and via FROG retrieved pulse comb (right) of the hybrid mode-locked device with 60 mA SGS current and  $-8$  V SAS reverse bias multiplexed up to around 160 GHz.

## 6. Conclusion

The pulses of the 40 GHz passive and hybrid QD-MLL have been characterized in dependence of the values of the SGS current and SAS reverse bias using the FROG technique. It was possible to gain insight into the device dynamics and to determine the influence of SGS current and SAS reverse bias on the pulse intensity profile and the chirp due to the carrier dynamics of the wetting layer and the dynamic equilibrium between the two sections. Larger SGS current increases the linear spectral chirp whereas increasing the SAS reverse bias leads to a decreasing linear spectral chirp until the influence of the QCSE becomes important.

Hybrid mode locking is shown to optimize the pulse shape by slightly suppressing side lobes on the trailing edge, in addition to a strong decrease of the jitter. We demonstrated experimental chirp compensation with a pulse FWHM of down to 700 fs in agreement with our theoretical predictions. An overall locking range of 101 MHz is achieved. Finally, we demonstrated the suitability of the QD-MLL for OTDM-based optical communication up to 160 Gbit/s.

### **Acknowledgment**

This work was supported by the research center SFB 787 of the German Research Foundation (DFG). The authors would like to thank Innolume GmbH, Dortmund, for the MBE growth of the wafers, as well as A. Steffan and A. Umbach from u2t photonics, Berlin, Germany, for the packaging of the MLL module.